



Sol–gel synthesis and electrochemical characterization of Mg-/Zr-doped LiCoO₂ cathodes for Li-ion batteries

F. Nobili^{a,*}, F. Croce^b, R. Tossici^a, I. Meschini^b, P. Reale^c, R. Marassi^a

^a Scuola di Scienze e Tecnologie, Sezione Chimica, Università degli Studi di Camerino, Via S. Agostino, 1, I-62032 Camerino (MC), Italy

^b Dipartimento di Scienze del Farmaco, Università 'G. D'Annunzio' Chieti-Pescara, Via dei Vestini, 31, I-66100 Chieti (CH), Italy

^c Dipartimento di Chimica, Università 'La Sapienza', P. le A. Moro, 5, I-00185 Roma, Italy

ARTICLE INFO

Article history:

Received 5 August 2011

Received in revised form 8 September 2011

Accepted 16 September 2011

Available online 21 September 2011

Keywords:

Sol–gel synthesis

Aliovalent doping

Cobaltite cathodes

Li-ion batteries

Electrochemical impedance spectroscopy

ABSTRACT

The complex sol–gel technique is applied to the preparation of Mg-/Zr-doped LiCoO₂ cobaltites. The synthesis results in composite powders in which the cathodic material is intimately mixed with inactive metal oxides as Co₃O₄, MgO and ZrO₂. Cycling ability of the electrodes is evaluated by chronopotentiometry at different currents and potentials, revealing an improved stability of the electrode surface for the Mg-/Zr-doped cathode. Kinetics is investigated by cyclic voltammetry and electrochemical impedance spectroscopy, revealing improvements both in bulk and interfacial transport properties. This behavior can be explained by the concomitant effects of Zr⁴⁺ doping and of morphology modifications induced by inactive MgO and ZrO₂ oxides dispersion.

© 2011 Elsevier B.V. All rights reserved.

1. Introduction

Since the first commercialization of lithium ion batteries and despite strong efforts in searching for alternative materials, cobaltite LiCoO₂ has been the preferential cathode compound for these devices. The performances of LiCoO₂ cathodes are mainly due to their layered structure that allows a relatively fast solid-state Li-ion diffusion and a high working potential (about 3.9 V vs. Li⁺/Li couple) [1–3]. Nevertheless, LiCoO₂ and iso-structural LiMO₂ analogues suffer from some limitations. In fact, their useful capacity hardly exceeds 50% of the theoretical value since only about 0.5 Li atoms per unit formula can be reversibly deintercalated/intercalated without causing irreversible structural changes that block further Li⁺ diffusion [4]. Moreover, it has been observed that the presence in the electrolyte solution of HF (which can be formed due to LiPF₆ decomposition induced by moisture) can cause the dissolution of the cathode and an extensive capacity fade [5,6].

Finally, some debate exists about the influence of the electronic conductivity of these compounds on the cathode performances, since a large variation of this physical quantity is usually observed during charge and discharge processes, especially at intercalation levels (*x* in Li_{*x*}MO₂) between 1 and 0.9 [7–10].

Different approaches have been followed to overcome these limitations and to improve the performances of layered cathodes. One of these involves the preparation of composite electrodes in which the particles of the active LiMO₂ material are coated by layers of metal oxides or other inactive phases (as TiO₂, Al₂O₃ and ZrO₂) [11–19]. The presence of such a coating can improve the stability of the electrode surface by preventing the reaction between the Co⁴⁺ ions and the electrolyte decomposition products, maintaining at the same time Li⁺ ionic conduction pathways. Inactive nanosize oxides can also be uniformly dispersed in the matrix of the electrode during the synthesis of the active material by co-precipitation of a secondary inactive phase. The foreign inactive oxide particles can be effective in stabilizing morphology of the active material by inhibiting its grain growth during the high temperature sintering step. Moreover, the defective surface of the foreign oxide particles can create 'nanoscale-interconnected' ionic conduction pathways that enhance the lithium diffusivity, thus improving the charge/discharge performances [20,21].

An alternative, conceptually different, route commonly followed to improve the LiCoO₂-based cathodes performances involves doping with aliovalent cations such as Mg²⁺. This can modify the valence states of both Co and O with charge compensation mechanisms that enhance the electronic conductivity of the host structure. In addition, it has been shown that the doped material remains single phase throughout the charge–discharge cycles, and its stability toward the electrolyte is increased [17,22–26]. All these factors concur in improving long-term stability and cycleability, at

* Corresponding author. Tel.: +39 0737 402210; fax: +39 0737 402296.
E-mail address: francesco.nobili@unicam.it (F. Nobili).

the expenses of only a minor capacity loss due to a slight decrease of active Co^{3+} concentration. Other doping attempts, with controversial results that depend also on the different synthetic approaches followed, are reported in the literature with cations as Ti^{4+} , Zr^{4+} , V^{5+} and Mo^{6+} that exhibit a nominal charge higher than Co^{3+} [27–30]. Mixed Ni–Co, Ni–Mn and Ni–Co–Mn cobaltite-type materials have been successfully doped with Zr^{4+} as well [31,32].

In previous papers [33–35] we have studied the electronic and ionic transport properties of cathode materials of general formula $\text{LiCo}_y\text{Ni}_{1-y}\text{O}_2$ ($0.2 < y < 1$) by electrochemical impedance spectroscopy (EIS). We have shown that the intercalation/deintercalation reaction involves both surface and bulk processes related, respectively, with the exchange of Li^+ ions at the electrode surface and with the conduction of electrons through the host lattice. Particularly, it has been shown that the reversible insulator-to-metal transition that usually takes place for this class of compounds in the very early stages of deintercalation [36] causes a large variation of the low-frequency region of the ac-impedance spectra. In fact, the low-frequency semicircle, attributed to the bulk electronic resistance of the material, undergoes a contraction of several order of magnitude when very small amounts of Li are extracted from the cathode. This behavior has been correlated with changes in cell parameters, particularly of the M–M in-plane distance ($M = \text{Co}, \text{Ni}$), that take place upon intercalation and deintercalation [9,37,38], by in situ X-ray diffraction measurements [39]. The analysis of ac-impedance spectra recorded at different temperatures has confirmed that this transition is related to a thermally activated electron conduction mechanism [40].

The proposed model has been further confirmed by a study of Mg-doped $\text{LiCo}_{0.95}\text{Mg}_{0.05}\text{O}_2$ cathodes [41]. A marked increase of bulk electronic conductivity with respect to the un-doped material has been found all over the entire intercalation degree range examined. Moreover, the insulator-to-conductor transition is promoted and restricted to the very early stages of the deintercalation process.

In this context, the present work reports the synthesis and the structural, morphological and electrochemical characterization of mixed Mg- and Zr-doped LiCoO_2 electrodes, focusing on the influence of doping on the charge–discharge performances and on the interfacial properties.

2. Experimental

The doped cobaltites were synthesized by sol–gel method [18,42], using $\text{Co}(\text{NO}_3)_3 \cdot 6\text{H}_2\text{O}$, LiNO_3 , $\text{Mg}(\text{NO}_3)_2 \cdot 6\text{H}_2\text{O}$ and $\text{Zr}(\text{OH})_n(\text{CH}_3\text{OO})_m$ as metal ions sources, citric acid as complexing agent and ethylene glycol as solvent (all materials from Sigma–Aldrich). The total amounts of M precursors ($M = \text{Co}, \text{Mg}, \text{Zr}$) have been used in slight, controlled excess with respect to the Li source. As a consequence, the excess of M^{n+} cations allowed the formation of small amounts of dispersed Co_3O_4 , ZrO_2 or MgO oxides as by-products of the syntheses. The gels were dried by using a controlled temperature ramp ranging 20–250 °C, until solid precursors were formed. The precursors were then ground and transferred to alumina boats for calcination and annealing in a furnace, under air atmosphere, following two subsequent temperature ramps from 20 to 300 °C and from 300 to 750 °C. The powders were accurately ground between the two heating ramps. For sake of comparison, un-doped LiCoO_2 was synthesized in the same conditions. The elemental ratios of the final materials were determined by atomic absorption spectrometry (AA) and inductively coupled plasma (ICP). The structure and the relative amounts of the synthesized phases were evaluated by X-ray powder diffraction (XRD) using a Ultima+ diffractometer (Rigaku, Japan) in θ/θ conventional Bragg–Brentano geometry, equipped

with a Cu-K_α source and a monochromator of the diffracted radiation.

All the electrodes were prepared by grinding in a mortar 80% active material, 10% carbon (Super-P by MMM Carbon), 10% plasticizer (PVdF by Aldrich) and then adding few drops of N-methyl-2-pyrrolidinone (by Aldrich) to form a suspension in a vial. After stirring, few drops of the suspensions were poured onto Al disks used as current collectors (diameter = 9 mm, by Alfa). The electrodes were first dried at 70 °C open air and then overnight at 120 °C under vacuum, and finally cold pressed at 8 tons cm^{-2} . The final loading of the electrodes resulted in the range 4–6 mg cm^{-2} of active mass. Morphologies of powders and electrodes have been investigated using a Morgagni Series 268D (FEI, Brno, Cheka Republic) transmission electron microscope (TEM) and a Cambridge Stereoscan mod. 360 scanning electron microscope (SEM).

T-shaped polypropylene Swagelok type cells, equipped with stainless steel (SS304) current collectors, were assembled in an Ar-filled dry-box with moisture and oxygen contents below 10 ppm, by using high-purity Li (Foote Mineral Co.) disks as counter and reference electrodes. 1 M LiPF_6 in EC:DEC:DMC 1:1:1 (Ferro Co.) was used as electrolyte. Polypropylene film (Celgard 2300) was used as separator.

All the electrochemical measurements were performed using a VMP2/Z electrochemical workstation (Bio-Logic SaS, France) at a temperature of 20 °C. Cyclic voltammetries were performed at 10 $\mu\text{V s}^{-1}$ scan rate, in order to ensure quasi-equilibrium conditions for the electrodes. Galvanostatic charge–discharge cycles were run by applying suitable currents in the desired potential ranges. Electrochemical impedance spectra were recorded in the frequency range 3 mHz to 100 kHz by superimposing a 5 mV sinusoidal perturbation to the bias potential. For sake of comparison, all the results obtained have been normalized to the active masses of the electrodes. All the potentials are given vs. Li^+/Li semi-couple.

3. Results and discussion

3.1. Structure and morphology

Fig. 1 shows the X-ray diffraction profiles of the synthesized powders. The main reflections, indexed according to Miller's notation, can be attributed to doped and un-doped LiCoO_2 phase, that crystallizes in an $R\text{-}3m$ space group isostructural with layered $\alpha\text{-NaFeO}_2$, in which Co (or the substitutional Zr), Li and O occupy, respectively, 3a, 3b and 6c sites. The extra diffraction signals are related to some amounts of inactive M (Co, Mg or Zr) oxides that are finely dispersed into the active materials. They are formed as by-products in all the syntheses because of the controlled doping cations excess added and of the Li tendency to form small amount of Li_2O , that eventually sublimates during annealing. This leads to an excess of M oxides in the final stoichiometry of the composite products. The theoretical angles of the related reflections are shown in Fig. 1 below the experimental diffraction profiles.

Table 1 reports the compositions of the powders as calculated by elemental analysis and profile matching of the XRD data, as well as the calculated structural and morphological parameters. The expansion of unit cell parameters a and c and volume V for samples B and C confirms that Zr^{4+} ions (0.87 Å), with larger ionic radii, did indeed substitute Co^{3+} ions (0.65 Å) in vacant 3a Wyckoff sites, rather than forming secondary Li_2ZrO_3 phase as were the cases reported by Needham et al. [29] and Luo and Dahn [30]. The cell expansion as a consequence of Zr^{4+} doping is consistent with several literature data [28,31,32] that report the structural parameters of Zr-doped cobaltites LiMO_2 ($M = \text{Co}, \text{Ni-Co}, \text{Ni-Co-Mn}$).

The values of c/a ratios found were consistently higher than 4.899 testifying a low degree of trigonal phase distortion and the

Table 1
Summary of structural and morphological parameters of samples A, B and C.

Sample Composition	A LiCoO ₂ (98.6%); Co ₃ O ₄ (1.4%)	B LiCo _{0.92} Zr _{0.08} O ₂ (95%); ZrO ₂ (5%)	C LiCo _{0.94} Zr _{0.06} O ₂ (98.3%); MgO (0.2%); ZrO ₂ (1.5%)
a (Å)	2.816	2.816	2.818
c (Å)	14.053	14.059	14.074
c/a ratio	4.990	4.993	4.996
V (Å ³)	96.506	96.547	96.787
Particle size (nm)	173	73	69

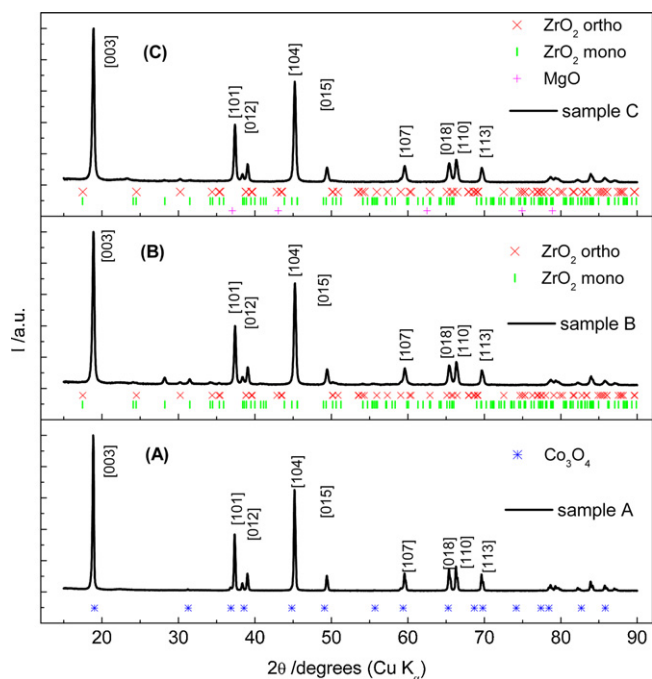


Fig. 1. XRD patterns of the samples under examination. Solid lines represent the experimental diffraction profiles. Main reflections of LiCoO₂ structures are indexed. (*), (x), (l) and (+), respectively, represent the theoretical reflections for Co₃O₄, orthorhombic ZrO₂, monoclinic ZrO₂ and MgO.

lack of significant cation disorder for all the synthesized doped and un-doped cobaltites [4,29].

As regards the minor phases dispersed in the composites, sample A contains only pristine LiCoO₂ with a slight amount of cobalt oxide Co₃O₄ (1.4%, w/o). Sample B, prepared by using a large excess of Zr precursor, contains a relatively high amount of Zr as doping cation entered into the active material structure and, at the same time, a relevant excess of dispersed ZrO₂ in both orthorhombic and monoclinic forms. The composition of the sample has been evaluated as LiCo_{0.92}Zr_{0.08}O₂:ZrO₂ 95:5 (w/o). Sample C, prepared by using lower amounts of both Mg and Zr precursors, resulted in LiCo_{0.94}Zr_{0.06}O₂:MgO:ZrO₂ 98.3:0.2:1.5 (w/o). A fraction of the added Zr atoms substituted Co atoms in the lattice of the host LiCoO₂ and the remaining fraction formed inactive ZrO₂ oxides, while Mg atoms only formed dispersed MgO. This suggests that, in the experimental conditions adopted, Zr can substitute Co in 3a sites more easily than Mg.

In the case of LiCoO₂ doping with Mg²⁺ the charge compensation mechanisms implies substitution of Co³⁺ ions with Co⁴⁺ ions or the creation of oxygen vacancies [22,38,41]. In the present case, where Zr⁴⁺ substitutes Co³⁺, formation of minor amounts of a lithium deficient Li_{1-x}MO₂ phase is hypothesized [29]. This is in agreement with Cho et al. [19], who speculate that nominally pure LiCoO₂ is defective, containing small amounts of Co⁴⁺, and is consistent with XRD results. In fact, as evidenced by Levasseur et al. [43],

Li-deficient cobaltite phase is characterized by an increase of both a and c cell parameters.

Fig. 2a, b and c shows transmission electron micrographs of powders A, B and C, respectively. All the powders appear to be sub-micrometric. The values of particle sizes, as evaluated by XRD data using Scherrer's formula, are listed in Table 1. For sample A an average particle size of about 175 nm has been calculated, while samples B and C retain average sizes below 100 nm. This behavior can be explained as an effect of the ZrO₂ and MgO oxides dispersed in the composite, that inhibit the aggregation of active material grains [20,21].

The morphology of the electrodes is consistent with that of the powders, as appears in Fig. 2d, e and f, that shows the scanning electron micrographs of the electrodes prepared from powders A, B and C, respectively. All the electrodes appear to be formed of sub-micrometric grains. Some aggregations occur only in electrode A.

3.2. Charge–discharge performances

Cycling behavior was evaluated in the potential range 3.6–4.2 V at C/5 charge/discharge rate. The 'useful' capacity has been considered as 50% of the theoretical value. In fact, as already reported in Section 1, layered Li_xMO₂ cathodes are usually reversibly charged and discharged only in the intercalation degree range 0.5 < x < 1. Thereafter, the cycling rates will be referred to this 'useful' capacity. Fig. 3a and b shows the discharge capacity values and the third cycle galvanostatic profiles for electrodes A, B and C. Electrodes A and C exhibit capacities of the order of 120–130 mAh g⁻¹, quite close to the 'useful' theoretical value of 137 mAh g⁻¹ for an x variation in the range 1–0.5. The composite electrode C (LiCo_{0.94}Zr_{0.06}O₂/MgO/ZrO₂) shows higher capacity than pristine LiCoO₂. On the contrary, electrode B (LiCo_{0.92}Zr_{0.08}O₂/ZrO₂) delivers a much lower capacity, with a more pronounced capacity fade upon cycling. This behavior is probably due to the relatively large amount (about 5%) of ZrO₂ that introduces inhomogeneities in the electrodes by electrically insulating some portions of the active material.

Based on these results, electrodes A and C have been selected for further electrochemical investigation. The electrodes have been cycled in several different operating conditions, in order to evaluate their charge–discharge performances and stability over larger potential windows and toward higher currents.

The capacity has been evaluated either by increasing the current up to 1C rate or by raising the charge cut-off potential of the cells up to 4.5 V. By increasing the charge/discharge rate a reduction of the reversible capacity is expected, since the increasing Ohmic polarization forces the electrodes to reach prematurely the cut-off potential, interrupting the charge process. Increase of the upper cut-off potential has at least two effects which have the tendency to balance themselves. The extension of the cycling potential window permits to exchange higher Li amounts but also negatively affects electrode stability, since Co⁴⁺ ions may react with electrolyte and distortions of the CoO₆ octahedra may occur, promoting a phase transition that eventually disrupts the intercalation framework and reduces the electrode cycling ability [6,44].

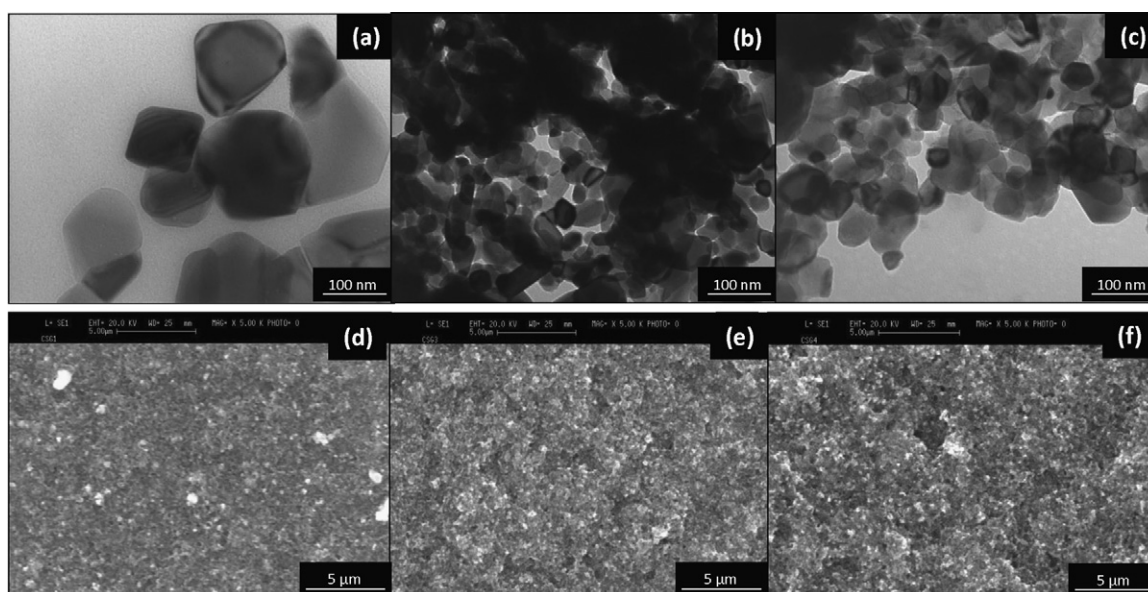


Fig. 2. (a–c) TEM micrographs of powders A, B and C. (d–f) Secondary electron SEM micrographs of electrodes A, B and C.

Table 2

Average discharge capacity of electrodes A and C as a function of the charge/discharge rate and of the potential window applied.

Electrode	Potential window (V)	3.6–4.2			3.6–4.35			3.6–4.5		
		C/5	C/3	C	C/5	C/3	C	C/5	C/3	C
		Capacity (mAh g ^{−1})								
A		109	102	89	131	115	49	134	93	5
C		113	100	90	128	118	88	129	122	111

Fig. 4a–c shows the intercalation capacities of the electrodes at the different C-rates and potential windows. Similar values (not shown here for sake of clarity) were obtained during the corresponding charge steps, since the charge/discharge processes have a Coulombic efficiency close to unity. When the electrodes are cycled utilizing a 3.6–4.2 V potential window (Fig. 4 panel a), the performances of the un-doped and doped electrodes A and C are comparable, even if at 1C charge/discharge rate the capacity fade for the doped electrode is less pronounced. A similar behavior has

been found by applying a 3.6–4.35 V potential window (Fig. 4 panel b). Under these experimental conditions, the capacity of the doped electrode is about twice that of the un-doped one at 1C rate. This latter result shows that when more ‘demanding’ operating conditions are applied, the doped electrode C benefits by a better stability. This behavior has been confirmed by increasing the upper cut-off potential up to 4.5 V (Fig. 4 panel c). In these conditions the performances of electrodes A and C are comparable only at C/5 charge/discharge rate. At C/3 rate the un-doped electrode exhibits a much more

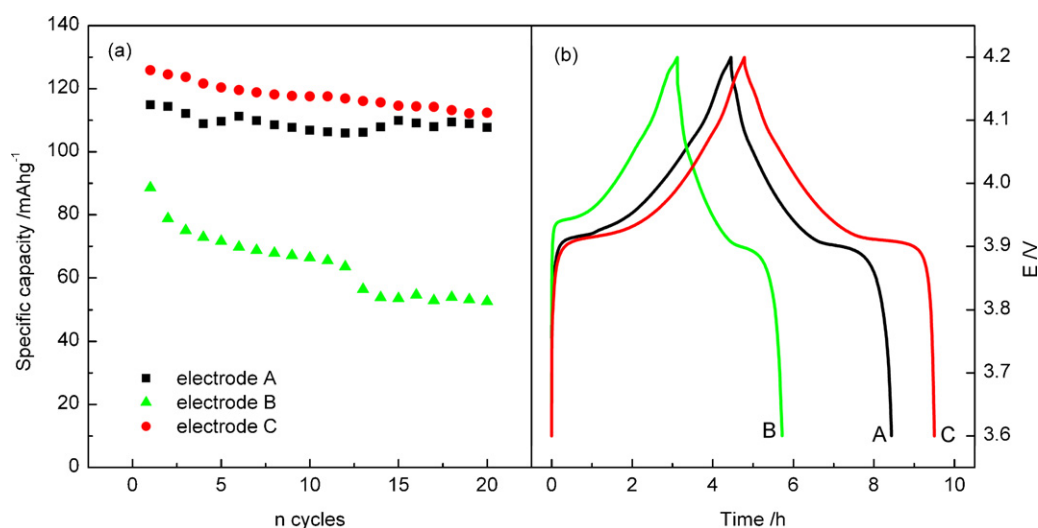


Fig. 3. (a) Specific capacity values of electrodes A, B and C. (b) Third-cycle galvanostatic charge/discharge profile for electrodes A, B and C. Charge/discharge rate = C/5, 3.6 < E < 4.2 V.

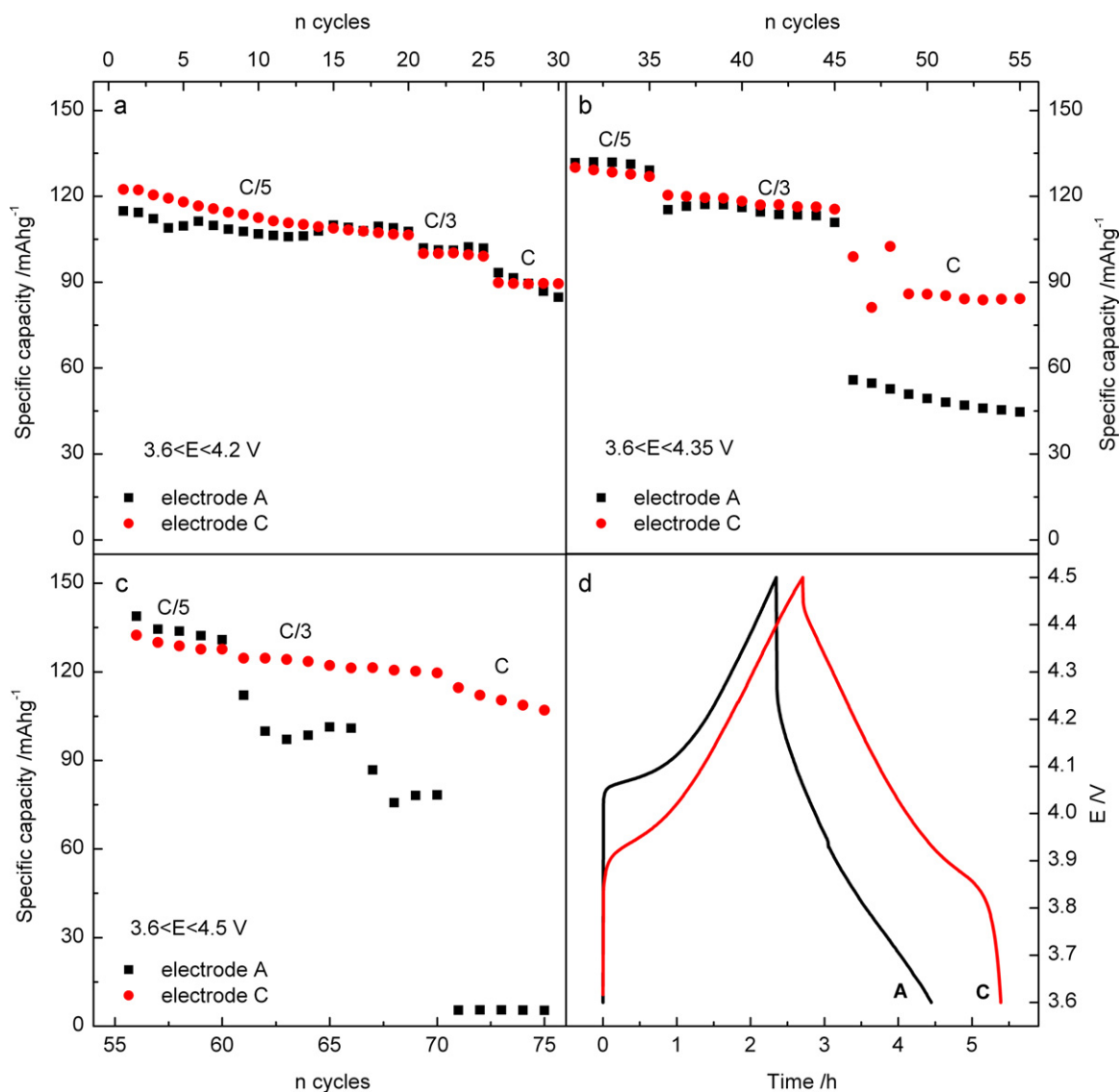


Fig. 4. Discharge capacity of electrodes A and C as a function of charge/discharge rate applied. (a) $3.6 < E < 4.2$ V, (b) $3.6 < E < 4.35$ V and (c) $3.6 < E < 4.5$ V. (d) Galvanostatic profiles for electrodes A and C. Charge/discharge rate = C/3, $3.6 < E < 4.5$ V.

pronounced capacity fade, and at 1C rate it is unable to exchange any useful amount of Li. On the contrary, the doped electrode at 1C rate still retains about 80% of the C/5 capacity. These results show that in the case of the Zr-doped electrode the potential window under which the electrode is cycled can be safely extended up to 4.5 V, demonstrating the improved stability of the cathode structure and surface. Fig. 4d shows the galvanostatic intercalation/deintercalation profiles of electrodes A and C recorded at C/3 rate and in the potential range $3.6 < E < 4.5$ V. The average discharge capacity values, obtained in the described experimental conditions, are summarized in Table 2.

3.3. Cyclic voltammetry

The intercalation/deintercalation kinetics of electrodes A and C has been investigated by slow-scan rate cyclic voltammetry (SSCV).

Fig. 5 shows the cyclic voltammograms of electrodes A and C acquired at a scan rate of $10 \mu\text{Vs}^{-1}$ during first and second cycles. The doped electrode C exhibits sharper voltammetric peaks than un-doped electrode A, reflecting faster intercalation/deintercalation kinetics.

The shapes of both curves closely resemble those reported in the literature by several authors who studied the electrochemical behavior of LiCoO_2 -based electrodes [7,45]. For both electrodes the peak related to the main process (about 3.92 V) undergoes a potential shift between first and second cycle. This may be ascribed to the occurrence of an initial irreversible ‘activation process’, commonly found for layered $\text{LiCo}_{1-y}\text{M}_y\text{O}_2$ cathodes and attributed to the formation of an electrode/electrolyte interphase layer [33,46]. Electrode C shows a lower potential shift than electrode A, probably reflecting the increased surface stability, due both to Zr-doping and to inactive MgO and ZrO_2 dispersions. The following cycles (not reported here) reflect the profiles of the second cycle.

Both electrodes show small peaks at about 4.07 and 4.17 V, that are commonly attributed to reversible phase transitions between ordered and disordered Li^+ arrangements in the host $[\text{Co}(\text{Zr})\text{O}_2]$ framework [10,29,47].

Because of the very low scan rate, the voltammetric profiles may be used, after integration, to estimate the dependence of the intercalation degree x on electrode potential. For both electrodes, the onset potential of the main intercalation peak (about 3.84 V) corresponds to an intercalation degree $x = 0.98$, while at peak potentials

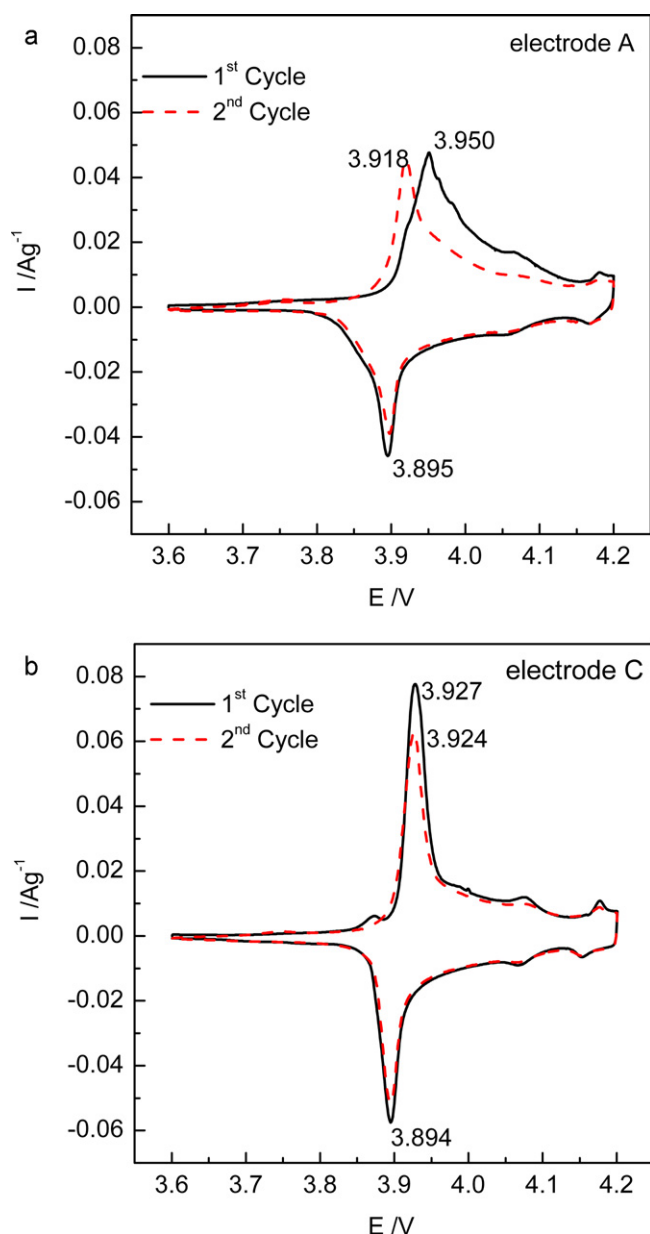


Fig. 5. First and second cyclic voltammograms of electrodes A (panel a) and C (panel b). Scan rate = $10 \mu\text{V s}^{-1}$. Peak potentials are pointed out.

(respectively 3.918 and 3.924 for electrodes A and C) the intercalation degree is $x = 0.88$.

3.4. Electrochemical impedance spectroscopy

Electrochemical impedance spectroscopy (EIS) has been applied in order to investigate the reasons for the improved kinetics of Zr-doped electrode C with respect to the un-doped one A. Fig. 6a–d shows sequences of Nyquist plots obtained with electrodes A and C at 20°C and at different potentials in the range 3.6–4.1 V. This corresponds approximately to an intercalation degree range between 1 and 0.57. All the spectra show the typical features of layered $\text{LiCo}_{1-y}\text{MyO}_2$ oxides previously studied [33–35,39]. At potentials far from the deintercalation peak, a great semicircular arc in the low-frequency region, that tends to close onto the real axis as the potential is increased, characterizes the spectra. For all the investigated potentials, a not well-defined arc can be identified in the high-frequency region, indicating the presence of a solid electrolyte

interphase (SEI). As the potential approaches the deintercalation peak, the diameter of the low-frequency semicircle decreases, and a middle-frequency semicircle, previously hidden, becomes more evident. At the same time a 45° line, characteristic of ionic diffusion, appears at the low-frequency limit. The overall impedances of both electrodes rapidly drop as the deintercalation proceeds. The same trend has been observed by reversing the scan and monitoring the intercalation process. This proves that the processes described in the ac-dispersions are reversible and that the fully intercalated phase can be restored during discharge, contrary to the behavior reported by Nishizawa et al. [48] and Shibuya et al. [10], but in agreement with previous results obtained on several $\text{LiCo}_{1-y}\text{MyO}_2$ samples [33–35].

All the ac-dispersions have been fitted to the equivalent circuit shown in Fig. 7. The circuit is the same used in previous papers to fit the frequency dispersions of the parent compound LiCoO_2 [39,40] and it is a modification of the one originally proposed by Bruce and Saïdi to describe the intercalation of Li^+ into TiS_2 according to an 'ad-atom model' [49]. In the original model proposed by Bruce and Saïdi the low-frequency resistance and capacitance were related, respectively, to the resistance encountered by Li^+ during the lattice incorporation and to the capacitance built-up during the adatom step. Moreover, the incorporation of Li^+ into the host lattice was considered the rate-limiting step of the overall intercalation process. In the present case, following previous interpretation of the ac-dispersions of LiCoO_2 [40,41], at potentials sufficiently lower than that of the main voltammetric peak the intercalation/deintercalation rate is extremely slow, and controlled by the electronic conductivity of the material. The low-frequency resistance and capacitance can thus be attributed to the bulk electronic resistance (R_{el}) and to an accumulation of charge at the surface of crystallites (C_{el}). The medium-frequency semicircle, that is the most relevant feature at potentials around the voltammetric peak, is related with the charge-transfer resistance (R_{ct}) and the associated double-layer capacitance (C_{dl}), while the high-frequency arc is attributed to the resistance and capacitance of the solid electrolyte interphase (R_{SEI} and C_{SEI}). A Warburg impedance (Z_W) in series with a differential intercalation capacity (C_i) is used to describe the low-frequency Li^+ solid-state diffusion inside the host lattice. The Boukamp's Equivalent Circuit program [50] has been used to fit the data. The values of χ^2 obtained, of the order of 10^{-5} , testify the good agreement between experimental and simulated data. In the simulations, Z_W and C elements were replaced by Constant Phase Elements Q [51] in order to take into account any deviations from the ideal behavior of the electrodes, usually caused by their inhomogeneity and roughness.

The high-frequency region is partly overlapped by the larger medium-frequency semicircle, so that the resistance of passivation layer (R_{SEI}) could only be roughly estimated. For both electrodes the values, not shown here, are practically invariant with the potential and of the order of few Ohms mg^{-1} .

Fig. 8a and b shows the calculated values for electronic (R_{el}) and charge-transfer (R_{ct}) resistances as a function of the electrodes potential. For both electrodes, the electronic resistance shows a dramatic drop at potentials lower than that of the intercalation peak. This latter corresponds to an intercalation degree range approximately between 1 and 0.9, confirming the results previously obtained [40,41] with doped and un-doped lithium cobalt oxides. This behavior, which is peculiar of this class of compounds, can be ascribed to a semiconductor-to-metal electronic transition. It should be noted that for the un-doped electrode A the electronic transition extends up to a potential of about 3.95 V, while for the doped electrode C it is complete at a potential of about 3.9 V. At higher potentials, for both electrodes the electronic resistance reaches a constant value. At 3.7 V (intercalation degree $x \sim 1$), the electronic resistance of the doped sample C is at least one order of

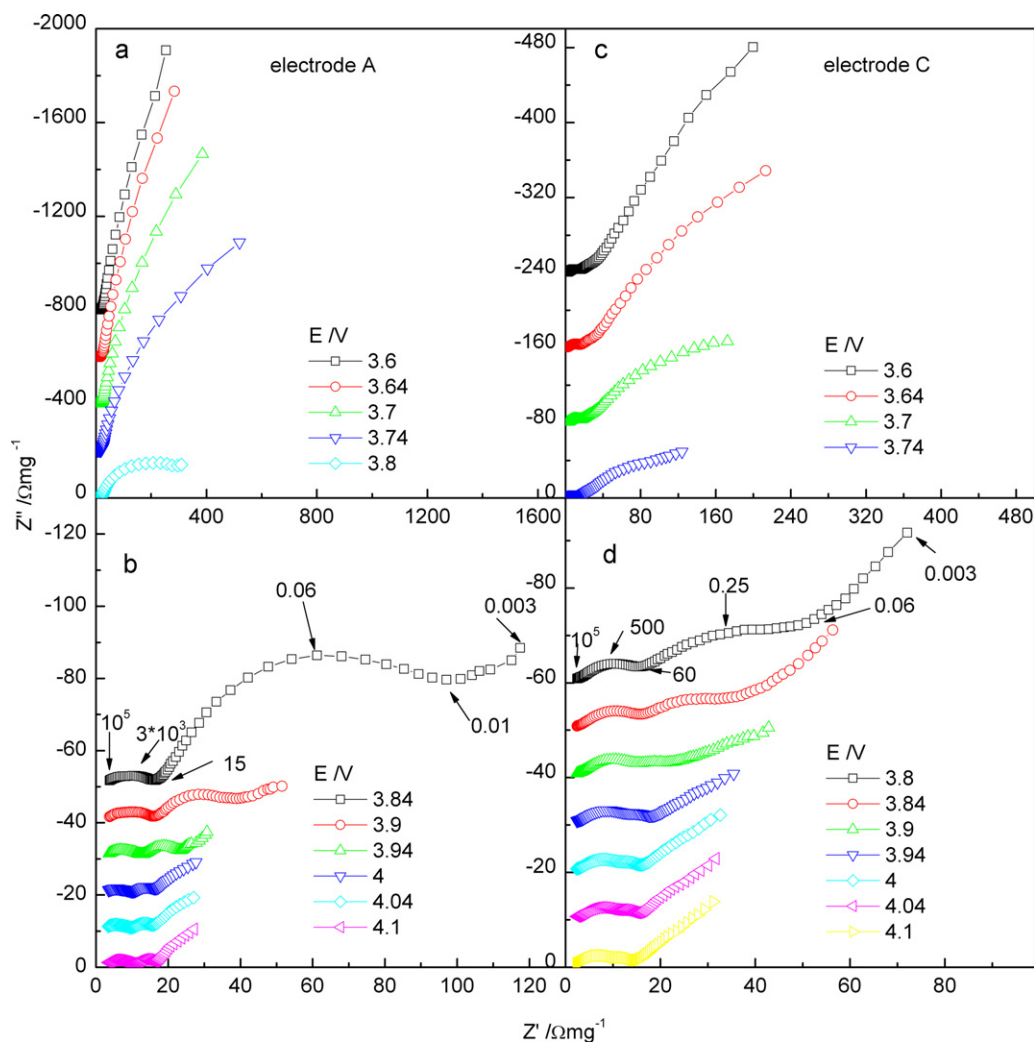


Fig. 6. Series of Nyquist plots obtained at different potentials for the LiCoO₂ electrode A (panels a and b) and for the composite MgO/ZrO₂/LiCo_{0.94}Zr_{0.06}O₂ electrode C (panels c and d). Characteristic frequencies (Hz) for the ac-dispersion recorded at 3.84 V are pointed out. 3 mHz < *f* < 100 kHz.

magnitude lower than that of the sample A. The difference becomes less significant as the deintercalation proceeds, but the electronic resistance of the doped sample shows lower values all over the potential range examined, even when the electronic transition is complete. These results confirm that, as it has been the case of other Co-substituted cobaltite cathodes [33–35,41], the introduction of aliovalent cations in the lattice leads to an overall increase of the material electronic conductivity.

The improved electronic transport properties of the doped electrode C can be explained by a mechanism similar to that proposed for Mg-doped LiCoO₂ [41], by which the electronic conductivity of the fully intercalated cobaltite is enhanced only in local domains around the doping cations. In the present case, the restricted conducting domains are located around Zr⁴⁺ ions or Li⁺ vacancies, and separated by bulk, poorly conducting, zones. As a consequence, the bulk properties of the fully intercalated cathode mostly reflect those of the poorly conducting parent material (as confirmed by lattice parameters *a* and *c* that increase only slightly), but, as the deintercalation proceeds, the insulator-to-conductor transition takes place in a very narrow *x* range, since the conducting domains become rapidly interconnected.

Both electrodes show a charge-transfer resistance, *R*_{ct}, almost constant for all the different intercalation degrees. This behavior implies that the rate-determining step of the overall electrochemical reaction does not involve the ‘classical’ charge-transfer of the

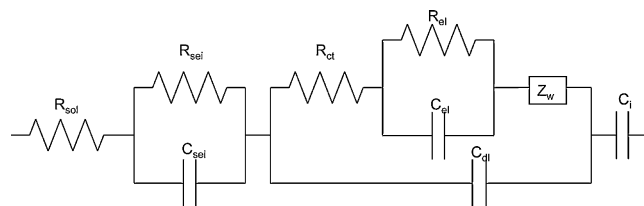


Fig. 7. Equivalent circuit used to fit the experimental ac-dispersions.

electron (as it is the case for conventional redox reactions on metal electrodes), but has to be ascribed to the Li⁺ ion desolvation step. The overall mechanism is analogous to that described with the ‘ad-atom’ model by Bruce and Saidi [49] which, in turn, had been previously proposed for other intercalation electrodes [33–35,52–54].

The absolute values of *R*_{ct} are similar for the electrodes A and C and much lower than those obtained, in the same experimental conditions, with commercial LiCo_{1–*y*}Ni_{*y*}O₂ oxides [35,40]. This behavior can be ascribed to the presence of inactive Co, Mg, Zr oxides. In fact, they interfere with the active material grain growth during the high temperature synthesis. This implies smaller grains of the active material, with a larger specific surface of the electrodes and an enhanced charge-transfer kinetics.

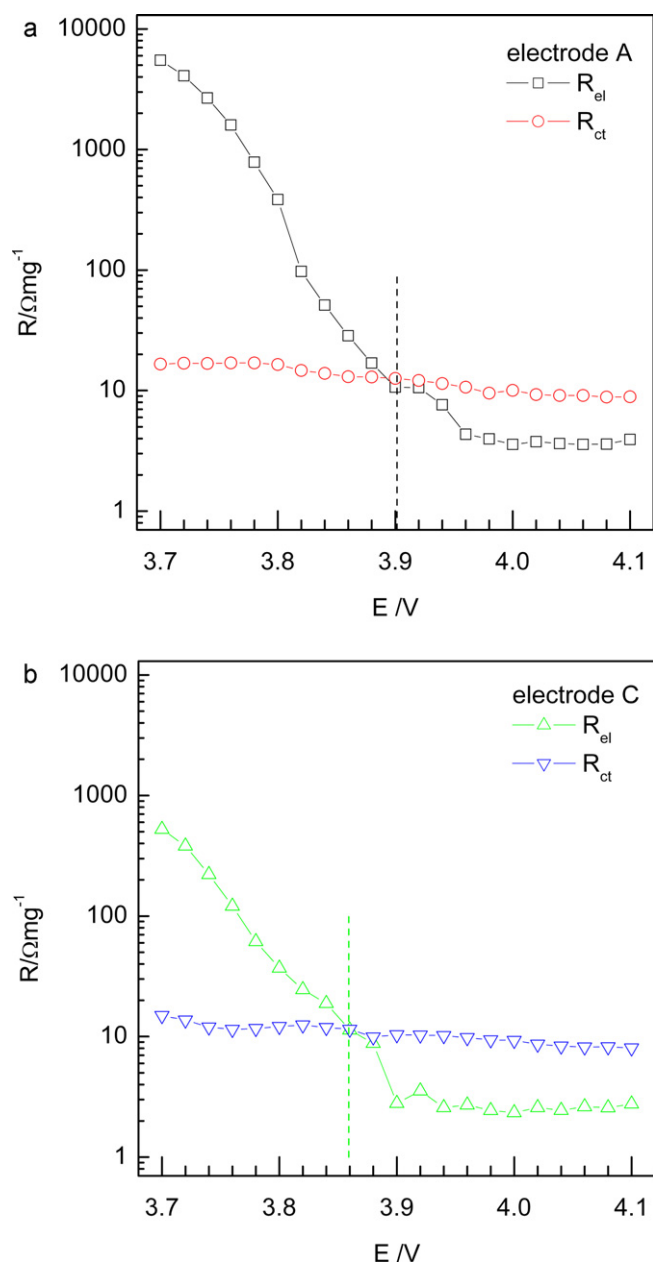


Fig. 8. Electronic resistance (R_{el}) and charge-transfer resistance (R_{ct}) for the LiCoO_2 electrode A (panels a and b) and for the composite $\text{MgO/ZrO}_2/\text{LiCo}_{0.94}\text{Zr}_{0.06}\text{O}_2$ electrode C (panels c and d).

For both electrodes, at the very beginning of the deintercalation process the electronic resistance, R_{el} , is higher than the charge-transfer resistance, R_{ct} . At potentials higher than 3.8 V R_{el} becomes lower than R_{ct} . This fact confirms that at the beginning of the deintercalation the overall electrode kinetics is controlled by the material electronic pseudo-hopping conductivity, while, when the insulator-to-conductor transition is complete, the kinetics is limited by interfacial phenomena, as already observed for Mg-doped and Ni-substituted cobaltites [35,41]. Moreover, the results here reported are in good agreement with those by Dokko et al. [7]. These authors did not include in the equivalent circuit a separate element to account for the electronic resistance. Nevertheless, they argued that the R_{ct} of a single-crystal LiCoO_2 electrode changed as a function of potential as a consequence of the variation of the lattice electronic conductivity.

4. Conclusions

Aliovalent metal doping of LiCoO_2 for Li-ion batteries cathodes has been pursued by sol-gel synthesis in which Mg and Zr precursors have been used in conjunction with Li and Co salts. Nanosize composite powders have been obtained, in which Co, Mg or Zr oxides have been formed as secondary phases together with undoped or Zr-doped cobaltites. The electrochemistry of the resulting composite samples obtained is strictly related to their chemistry and morphology. Particularly, the $\text{LiCo}_{0.94}\text{Zr}_{0.06}\text{O}_2/\text{MgO/ZrO}_2$ composite shows the best electrochemical performances when cycled at higher current rates and with higher potential cut-offs. This is probably due to a reduced grain size and a more stable structure and surface of the doped cobaltite, which in turn is caused both by the light Zr doping and by the MgO/ZrO_2 dispersion in active material.

Analysis of kinetics by cyclic voltammetry and impedance spectroscopy reveals an overall reduction of polarization for all the electrodes under examination, in particular for the Zr-doped cathode, with respect to larger-grain-size commercial cobaltite. The transition from semiconductor-to-metal electronic properties is confirmed to occur in the very early stages of deintercalation. For the Zr-doped sample, this transition extends over a narrower range of intercalation degree and leads to lower values of the material electronic resistance. This behavior is explained by the doping effect of Zr^{4+} ions and by the presence of Li defects, resulting in an enhanced electronic conductivity in local domains, which rapidly interconnect as Li^+ deintercalation takes place. At the peak deintercalation potential, for all the electrodes investigated the overall electrochemical kinetics is controlled by the interfacial ‘ad-atom’ step, which includes Li^+ ions desolvation.

Further investigations are currently in progress in order to evaluate the impact of different doping levels and different amounts of inactive oxides in the composites toward the electrochemical behavior of the electrodes.

Acknowledgements

This work was supported by ENI within the LiBEST project. The authors would like to thank Dr. Cecilia Paolini from ‘G. D’Annunzio University’ of Chieti-Pescara (Italy) for the kind support in TEM images acquisition and analysis.

References

- [1] K. Mitzushima, P.C. Jones, P.J. Wiseman, J.B. Goodenough, *Mater. Res. Bull.* 15 (1980) 783.
- [2] T. Nagaura, K. Tozawa, *Prog. Batteries Solar Cells* 9 (1990) 209.
- [3] K. Ozawa, *Solid State Ionics* 69 (1994) 212.
- [4] R. Alcantara, P. Lavela, J.L. Tirado, R. Stoyanova, E. Zhecheva, *J. Solid State Chem.* 134 (1997) 265.
- [5] Y.J. Kim, J. Cho, T.J. Kim, B. Park, *J. Electrochem. Soc.* 150 (2003) A1723.
- [6] G.G. Amatucci, J.M. Tarascon, L.C. Klein, *Solid State Ionics* 83 (1996) 167.
- [7] K. Dokko, M. Mohamedi, Y. Fujita, T. Itoh, M. Nishizawa, M. Umeda, I. Uchida, *J. Electrochem. Soc.* 148 (2001) A422.
- [8] M. Ménétrier, I. Saudoune, S. Levasseur, C. Delmas, *J. Mater. Chem.* 9 (1999) 1135.
- [9] J. Molenda, A. Stoklosa, T. Bak, *Solid State Ionics* 36 (1989) 53.
- [10] M. Shibuya, T. Nishina, T. Matsue, I. Uchida, *J. Electrochem. Soc.* 143 (1996) 3157.
- [11] Z. Chen, J.R. Dahn, *Electrochem. Solid-State Lett.* 5 (2002) A213.
- [12] J. Cho, Y.J. Kim, T.-J. Kim, B. Park, *Angew. Chem. Int. Ed.* 40 (2001) 3367.
- [13] J. Cho, Y.J. Kim, T.-J. Kim, B. Park, *Chem. Mater.* 12 (2000) 3788.
- [14] J. Cho, Y.J. Kim, T.-J. Kim, B. Park, *J. Electrochem. Soc.* 148 (2001) A1110.
- [15] S.-M. Park, T.-H. Cho, Y.-M. Kim, M. Yoshio, *Electrochem. Solid-State Lett.* 8 (2005) A299.
- [16] Y. Jin, N. Li, C.H. Chen, S.Q. Wei, *Electrochem. Solid-State Lett.* 9 (2006) A273.
- [17] M. Mladenov, R. Stoyanova, E. Zhecheva, S. Vassilev, *Electrochem. Commun.* 3 (2001) 410.
- [18] S.M. Lee, S.H. Oh, J.P. Ahn, W.I. Cho, H. Jang, *J. Power Sources* 159 (2006) 1334.
- [19] J. Cho, C.-S. Kim, S.-I. Yoo, *Electrochem. Solid-State Lett.* 3 (2000) 362.

- [20] J. Jamnik, R. Daminko, B. Erjavec, M. Remskar, A. Pintar, M. Gaberscek, *Adv. Mater.* 21 (2009) 2715.
- [21] Y.-S. Hu, Y.-G. Guo, R. Dominko, M. Gaberscek, J. Jamnik, J. Maier, *Adv. Mater.* 19 (2007) 1963.
- [22] H. Tukamoto, A.R. West, *J. Electrochem. Soc.* 144 (1997) 3164.
- [23] R. Thirunakaran, N. Kalaiselvi, P. Periasamy, N.G. Renganathan, *Ionics* 9 (2003) 388.
- [24] C. Julien, G.A. Nazri, A. Rougier, *Solid State Ionics* 135 (2000) 121.
- [25] S. Levasseur, M. Ménétrier, C. Delmas, *J. Power Sources* 112 (2002) 419.
- [26] C. Julien, M.A. Camacho-Lopez, T. Mohan, S. Chitra, P. Kalyani, S. Gopukumar, *Solid State Ionics* 135 (2000) 241.
- [27] M. Ganesan, *Ionics* 15 (2009) 609.
- [28] H.-S. Kim, T.-K. Ko, B.-K. Na, W.I. Cho, B.W. Chao, *J. Power Sources* 138 (2004) 232.
- [29] S.A. Needham, G.X. Wang, H.K. Liu, V.A. Drodz, R.S. Liu, *J. Power Sources* 174 (2007) 828.
- [30] W. Luo, J.R. Dahn, *J. Electrochem. Soc.* 158 (2011) A110.
- [31] S.H. Oh, S.M. Lee, W.I. Cho, B.W. Cho, *Electrochim. Acta* 51 (2006) 3637.
- [32] H.J. Bang, B.-C. Park, Y.-K. Sun, *J. Power Sources* 174 (2007) 565.
- [33] F. Croce, F. Nobili, A. Deptula, W. Lada, R. Tossici, A. D'Epifanio, B. Scrosati, R. Marassi, *Electrochem. Commun.* 1 (1999) 605.
- [34] F. Nobili, R. Tossici, F. Croce, B. Scrosati, R. Marassi, *J. Power Sources* 94 (2001) 238.
- [35] F. Nobili, F. Croce, B. Scrosati, R. Marassi, *Chem. Mater.* 13 (2001) 1642.
- [36] J. Molenda, *Solid State Ionics* 119 (1999) 19.
- [37] J. Molenda, *J. Phys. Stat. Sol. B* 165 (1989) 419.
- [38] J.B. Goodenough, in: H. Reiss (Ed.), *Progress in Solid State Chemistry*, vol. 5, Pergamon Press, Oxford, 1971, p. 279.
- [39] F. Nobili, S. Doske, M. Minicucci, F. Croce, R. Marassi, *J. Phys. Chem. B* 110 (2006) 11310.
- [40] F. Nobili, R. Tossici, R. Marassi, F. Croce, B. Scrosati, *J. Phys. Chem. B* 106 (2002) 3909.
- [41] F. Nobili, S. Dsoke, F. Croce, R. Marassi, *Electrochim. Acta* 50 (2005) 2307.
- [42] R. Alcántara, P. Lavela, J.L. Tirado, R. Stoyanova, E. Kuzmanova, E. Zhecheva, *Chem. Mater.* 9 (1997) 2145.
- [43] S. Levasseur, M. Ménétrier, E. Suard, C. Delmas, *Solid State Ionics* 128 (2000) 11.
- [44] S. Levasseur, M. Ménétrier, C. Delmas, *Chem. Mater.* 14 (2002) 3584.
- [45] M.D. Levi, G. Salitra, B. Markovsky, H. Teller, D. Aurbach, U. Heider, L. Heider, *J. Electrochem. Soc.* 146 (1999) 1279.
- [46] F. Croce, A. Deptula, W. Lada, R. Marassi, T. Olczak, F. Ronci, *Ionics* 3 (1997) 390.
- [47] T. Ohzuku, A. Ueda, *J. Electrochem. Soc.* 141 (1994) 3972.
- [48] M. Nishizawa, S. Yamamura, T. Itoh, I. Uchida, *Chem. Commun.* 16 (1998) 1631.
- [49] P.G. Bruce, M.Y. Saidi, *J. Electroanal. Chem.* 322 (1992) 93.
- [50] B.A. Boukamp, *Solid State Ionics* 20 (1986) 159.
- [51] E. Barsoukov, J.R. Macdonalds, *Impedance Spectroscopy. Theory, Experiment, and Applications*, 2nd edition, Wiley, New York, 2005, p. 39.
- [52] M. Mancini, F. Nobili, S. Dsoke, F. D'Amico, R. Tossici, F. Croce, R. Marassi, *J. Power Sources* 190 (2009) 141.
- [53] F. Nobili, S. Doske, M. Mancini, R. Marassi, *Fuel Cells* 9 (2009) 264.
- [54] F. Nobili, M. Mancini, S. Dsoke, R. Tossici, R. Marassi, *J. Power Sources* 195 (2010) 7090.